CRYSTAL GROWTH & DESIGN

Article

pubs.acs.org/crystal

Molecular Insights into Early Nuclei and Interfacial Mismatch during Vapor Deposition of Hybrid Perovskites on Titanium Dioxide Substrate

Jingfan Wang,[†] Lingling Zhao,*[,†] Mingchao Wang,[‡] and Shangchao Lin*[,‡]

[†]Key Laboratory of Energy Thermal Conversion and Control of Ministry of Education, School of Energy & Environment, Southeast University, Nanjing, Jiangsu 210096, China

[‡]Department of Mechanical Engineering, Materials Science & Engineering Program, FAMU-FSU College of Engineering, Florida State University, Tallahassee, Florida 32310, United States

Supporting Information

ABSTRACT: Theoretical understanding of the nucleus structures of hybrid perovskites, such as those of the prototypical methylammonium lead triiodide ($MAPbI_3$), can greatly improve the deposited thin film quality and the resulting optoelectronic device performance. In this paper, we report a systematic molecular dynamics simulation study on nucleation and interfacial mismatch during the vapor deposition of $MAPbI_3$ on the TiO_2 substrate under different ionic precursor (PbI_2 and MAI salts) compositions and temperatures. Despite significant anisotropic lattice mismatches, small defects are observed at the $TiO_2/[MAI]^0$ interface due to intermediate electrostatic attractions between I and Ti atoms, while very strong electrostatic attractions between Pb and O atoms lead to significant defects at the $TiO_2/[PbI_2]^0$ interface. From the vapor deposition simulations, we identify PbI_4^{2-} tetrahedra, PbI_5^{3-} pyramids, and PbI_6^{4-} octahedra as dominant polyhedral building blocks of early $MAPbI_3$ nuclei. Specifically, the PbI_5^{3-} pyramids dominate over other polyhedra and could be a good candidate for converting into PbI_6^{4-} octahedra upon further crystallization. We further identify early $MAPbI_3$ nuclei built upon well-connected PbI_x polyhedral clusters and finally locate the efficient early $MAPbI_3$ nuclei based on sufficient amounts of surrounding MA^+ cations. The populations of these early nuclei increase rapidly with increasing the MAI composition, suggesting that potential improvements in film quality could be introduced by depositing more MAI salts or MA^+ cations, a finding consistent with experiments. Although the impact from temperature is weaker than that from composition, the optimal temperature for nucleation is found to decrease with increasing the precursor composition PbI_2/MAI. Finally, the TiO_2 substrate leads to layered structures of ionic species close to its surface, but such ordering does not seem to promote prenucleation, which poses a need for the new design of substrates that are more compatible with PbI_6^{4-}-based early nuclei.

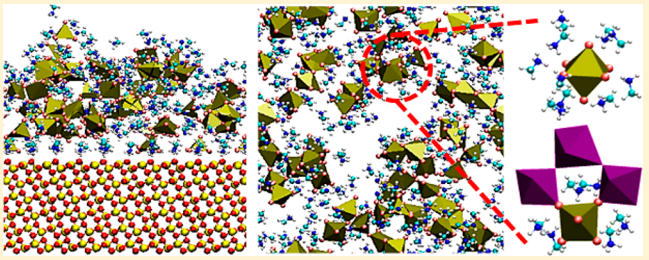

1. INTRODUCTION

Hybrid organometal halide perovskites (ABX_3) are double rock-salt structured ionic crystals composed of A^+ (organic), B^{2+} (metallic), and X^- (halide) ions, which allow integration of useful organic and inorganic characteristics within a single molecular-scale crystal, enabling unique electronic, thermal, and optical properties. ABX_3 semiconductors, such as the prototypical methylammonium lead triiodide ($CH_3NH_3PbI_3$ or $MAPbI_3$), have emerged as a promising class of multifunctional materials for a wide range of applications, such as photovoltaic (PV) solar cells, thermoelectric generators, and light-emitting diodes (LEDs).[1,2−5] These semiconductors have attracted increasing attention due to their scalable, low-temperature synthesis processes, small electron bandgaps, high light absorptivity, low thermal conductivity, and high carrier mobility.[3,6,7] The reported power conversion efficiency (PCE) of hybrid perovskite solar cells (PSCs) has significantly increased from around 12% to more than 20% in the past 4 years,[8−14] the highest values among emerging solar cells.[15] Very high PCEs have been achieved in planar-structured PSCs with stacked thin films of $MAPbI_3$ on a TiO_2 substrate,[16,17] where the wide-bandgap TiO_2 semiconductor[18,19] serves as an electron transporter. Together with the high open-circuit voltage and steep absorption edge, as well as high transparency for wide-range optical wavelengths >825 nm,[20] hybrid perovskite materials are viewed as competitive candidates for fabricating tandem cells with a potential PCE of over 30%.[21]

Over the past few years, planar-structured heterojunctions with a simple configuration have gradually become a preferred structure to choose for fabricating PSCs.[22−24] Considering the intimate structure−property-performance relationship in PSCs, high-quality perovskite films are essential to make efficient

Received: May 2, 2017
Revised: October 8, 2017
Published: October 27, 2017

DOI: 10.1021/acs.cgd.7b00626
Cryst. Growth Des. 2017, 17, 6201−6211

planar PSCs. Motivated by the above need, various techniques, such as physical vapor deposition (PVD),[22] solution engineering,[11,25] vapor-assisted solution deposition,[8] and sequential deposition,[14,26] have been explored to improve the various aspects of film quality, including uniformity, smoothness, and surface coverage. Lacking proper solvents, conventional solution-based methodologies with fast reaction between inorganic and organic species often result in perovskite films with incomplete coverage and unavoidable defects, such as pinholes. Furthermore, many research works demonstrated that novel solution-processing approaches could achieve improved films but with limited reproducibility.

On the other hand, vapor-based chemical deposition methods have been well-developed and extensively applied in thin-film solar cells (e.g., α-Si, graphene, and C_{60}),[27,28] organic light-emitting diode (OLED),[29] and liquid-crystal display industries. Dual-source vacuum evaporation has been proven to be competitive for the fabrication of planar-heterojunction PSCs by generating uniform and dense perovskite films and by optimizing the device's electronic transport properties via well-controlled composition. Luo et al.[23] reported another popular PVD technique employing MAI vapor being deposited into PbI_2 films, where the low-rate gas−solid reaction is similar to vapor-assisted deposition,[8] and they achieved a long electron diffusion length of 240 nm. Very recently, vacuum evaporation was also involved in the fabrication of a $MAPbI_3$/silicon tandem cell, delivering an exciting PCE of up to 21.2% by Werner et al.[30] Notably, during $MAPbI_3$ fabrications using the sequential deposition method, it was reported that the fast crystallization of PbI_2 would cause incomplete MAI-PbI_2 mixing, and consequently, the generated PbI_2 crystals with different sizes would result in an uncontrolled perovskite film morphology, which will deteriorate the reproducibility of PSCs.[14] Many researchers have also reported that adding more MAI salts could resist the generation of fast-forming edge-sharing octahedra typically observed in PbI_2 crystals. Snaith et al.[22] further noted that in their vapor deposition experiments, the optimal ionic precursor composition (i.e., the $PbCl_2$/MAI molar ratio) increases from 1:3.5 to 1:4, when the corresponding thickness of the deposited thin film increases from 125 to 330 nm.

Although extensive experimental studies have been carried out on PSCs, atomistic-level structures of hybrid perovskite nuclei and the perovskite−substrate interface during vapor deposition has yet been unexplored due to the lack of nanoscale theoretical and computational studies. Although first-principle density functional theory (DFT) calculations have been used extensively to study the electronic and optical properties of hybrid perovskites, simulations of the perovskite nucleation process require larger systems and faster algorithms. With the above in mind, we use classical molecular dynamics (MD) simulations to study the prenucleation steps of $MAPbI_3$ during the PVD process on a TiO_2 substrate under three controlled temperatures (300, 413, and 526 K) and three ionic precursor compositions (salt molar ratio PbI_2/MAI = 1:2, 1:1, and 2:1, with the total number of salt molecules fixed). After identifying the structural fingerprints of pristine $MAPbI_3$ crystal using radial distribution function, we investigated the structural stability of $MAPbI_3$ at the $[MAI]^0/TiO_2$ and $[PbI_2]^0/TiO_2$ interfaces under different temperatures. We further categorize various PbI_x polyhedra, well-connected PbI_x clusters, and early $MAPbI_3$ nuclei structures upon PVD, and finally, investigate their strong dependence on precursor composition. Finally, we discuss the impact from the TiO_2 substrate to the distributions of various ionic species and the formation of efficient early $MAPbI_3$ nuclei.

2. COMPUTATIONAL METHODS

All the MD simulations were carried out using the open-source LAMMPS[31] software package. The crystal structure of $MAPbI_3$ is shown in Figure S1a. The classical model potential for hybrid perovskites (named MYP) force field[32] is used to describe the complicated organometallic structure and interactions of $MAPbI_3$. The MYP force field was recently developed by Mattoni et al., which can nicely reproduce the temperature-dependent structural, dynamical, and physical properties of $MAPbI_3$, including phase diagram,[32] point-defect diffusivity,[33] atomic vibrations and phonon modes,[34] phonon transport and thermal conductivity,[35,36] electro- and mechanocaloric effects,[37] and solid fracture mechanics.[38] Details about the MYP force field are reported in ref 32. We choose the most stable anatase (101) TiO_2 surface[39] as the substrate for the PVD process and use the Matsui-Akaogi force field[40] to describe the interactions within TiO_2. Previous studies[41] have proved that this force field is able to reproduce the mechanical and structural properties of different types of TiO_2 crystals.

In summary, pairwise interactions between (Pb,I)-(Pb,I), (Pb,I)-(C,N), and (Ti,O)-(Ti,O) are described by Buckingham and Coulombic potentials, while Lennard−Jones (LJ) and Coulombic potentials are employed to define all the others. Specifically, the LJ parameters for the atoms in MA^+ ($CH_3NH_3^+$) cations are given by the AMBER[42] force field, while those for other atoms (Pb, I, Ti, and O) are listed in Table S1, based on refs 40 and 43−45. Note that the self-interacting LJ parameters for Pb and I are only used to derive the cross-term LJ parameters between (Pb,I)-(Ti,O) using the geometric-mean combining rule. Long-range electrostatic interactions are treated here using the particle mesh Ewald (PME) summation method.[46,47] The same cutoff distance of 1 nm is used for all short-range (Buckingham and LJ) and long-range (Coulombic) interactions. Periodic boundary conditions in all three dimensions and a timestep of 1 fs are applied in all the simulations.

To study the general mechanism of $MAPbI_3$ nucleation during the PVD, three model systems are investigated in this work. In the first model system, a pristine bulk $MAPbI_3$ crystal is built in a simulation box dimension of ~4.4 × 5.1 × 5.1 nm^3 (see Figure S1a for the initial configuration) to provide a baseline for the following structural comparison. In the second model system, we aim to study the structural stability of the two relatively stable, charge-neutral $[MAI]^0$- and $[PbI_2]^0$-terminated surfaces of $MAPbI_3$ interfacing with the anatase (101) TiO_2 surface (see Figure S1b for the initial configuration). A 2 nm-thick TiO_2 film is added in the second model system to interact with a $MAPbI_3$ crystal that is based on the same model used in the first model system, which results in a simulation box size of ~4.5 × 5.2 × 7.4 nm^3. After energy minimization, both first and second model systems are simulated under the NPT ensemble with an isotropic pressure of 1 bar (~ atmospheric pressure) and different temperatures (300, 413, and 516 K) for 20 ns using the Nosé−Hoover thermostat and barostat.[48,49] MD trajectories of the first model system during the last 10 ns is collected every 500 ps for data analysis, while those of the second model system during the last 5 ns are collected every 100 ps for data analysis.

As shown in Figure S1c, the third model system is used to simulate the PVD process, and PbI_2 and MAI salts are randomly inserted into a 1 nm thick lateral region, which is 3.5 nm above the top surface of the TiO_2 substrate with the same size as in the second model system. The size of the third model system is ~4.5 × 5.2 × 12.0 nm^3. To understand the dependence of $MAPbI_3$ nuclei formation during the PVD process on both temperature and ionic precursor composition, we studied three representative temperatures (300, 413, and 526 K) and precursor compositions for PbI_2/MAI (= 1:2, 1:1, and 2:1). Although Snaith et al.[22] water-cooled the substrate to 21 °C, we expect that the substrate−vapor interface would exhibit higher temperatures (such as 413 and 526 K studied here) due to convective and radiative

DOI: 10.1021/acs.cgd.7b00626
Cryst. Growth Des. 2017, 17, 6201−6211

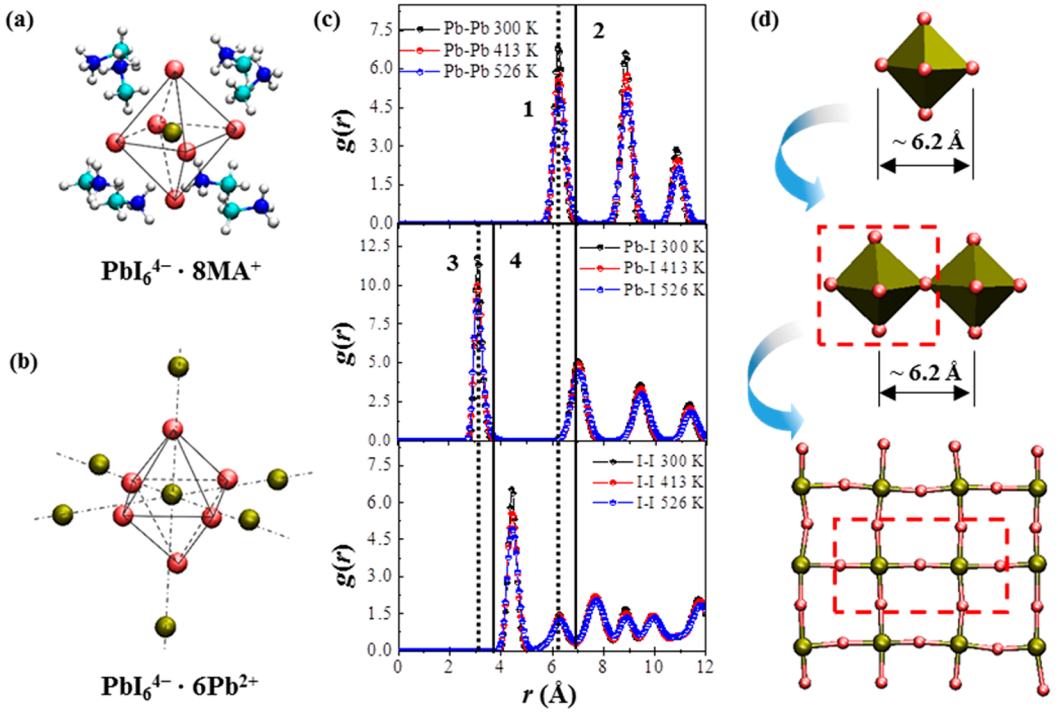

Figure 1. MD simulation snapshots of the detailed atomic structures of the octahedral PbI_6^{4-} framework with the surrounding: (a) 8 MA^+ and (b) 6 Pb^{2+} ions. (c) Simulated radial distribution functions (RDFs) for the Pb−Pb, Pb−I, and I−I pairs in a pristine bulk $MAPbI_3$ crystal. The four vertical lines (1-4) denote characteristic pair separation distances at r = 3.1, 3.8, 6.2, and 7.0 Å. (d) Lattice constant and structure of a PbI_6^{4-} octahedron. Two PbI_6^{4-} octahedra connect to each other by sharing one common I ion in a corner-sharing fashion. Color code: Pb − tan, I − pink, N − navy blue, C − light blue, H − white.

heat transfers at the interface under thermal equilibrium. In addition, within typical short time scale MD simulations (in tens of ns), the ionic species from the vapor would not be cooled down fast enough when they are in contact with the low temperature substrate, primarily due to limited thermal conductivity at the substrate−vapor interface within such a short time scale.

In all the PVD MD simulations, we deposited a fixed total number of 504 PbI_2 and MAI precursors (salt molecules) into the system. Four precursors are deposited every 100 ps during the PVD process. Note that this high frequency of deposition may lead to the clustering of amorphous $MAPbI_3$ far away from TiO_2, so an acceleration of 2.3 × 10^{-2} (nm/ps^2) along the $-z$ direction is constantly applied to each precursor atom to enhance direct contacts between $MAPbI_3$ and TiO_2. After the PVD process and energy minimization, the third model system is equilibrated under the $NP_{xy}T$ ensemble with a pressure of 1 bar controlled only along the x and y directions. The precursor PVD process lasts for 12.6 ns, and the equilibration lasts for another 40 ns to investigate early nucleus formation. For the third model system, MD trajectories during the last 20 ns are collected every 100 ps for further data analysis.

3. RESULTS AND DISCUSSION

3.1. Crystal Structure Fingerprints of Pristine Bulk Perovskites. Molecular dynamics of organic MA^+ cations in bulk $MAPbI_3$, in particular, their rotational motions, are reported to highly depend on temperatures, crystal phases, and the atomic structure of the surrounding inorganic Pb−I framework (see Figure S1a).[50−52] Therefore, we focused on the Pb−I framework as the structure fingerprint of bulk $MAPbI_3$ and calculated the radial distribution functions (RDFs) of the Pb−I frameworks at different temperatures. As shown in Figure 1a, each Pb atom is surrounded by six first nearest-neighbor I atoms, which form a Pb-centered octahedron, marked as the PbI_6^{4-} octahedron. As shown in Figure 1a,b, each Pb atom is also surrounded by 8 second nearest-neighbor MA^+ cations and 6 third nearest-neighbor Pb atoms.

The calculated pairwise Pb−Pb, Pb−I, and I−I RDFs at 300, 413, and 526 K are shown in Figure 1c. As the temperature increases, all the peaks in the RDF curves get slightly lowered and broadened, while their locations stay the same. The peak observed at 3.1 Å (line 3) in the Pb−I RDF features the first nearest-neighbor I atoms around Pb, while a cutoff distance of 3.8 Å (line 4) where the RDF becomes zero could be used for counting these I neighbors and plot the PbI_x polyhedra (or Pb neighbors if the I atom is the reference). The peak observed at 4.4 Å in the I−I RDF features the first nearest-neighbor I atoms around I (corresponding to the edge length of the PbI_x polyhedra), while a cutoff distance of 5.0 Å could be used for counting these I neighbors. The peak observed at 6.2 Å (line 1) in the Pb−Pb RDF features the first nearest-neighbor Pb atoms around Pb, while a cutoff distance of 7.0 Å (line 2) could be used for counting these Pb neighbors. According to these values, the ionic Pb−I bonds are the shortest and the strongest among all these types of pairwise interactions, from which we can conclude that the ionic Pb−I bond are the easiest-forming structure during the crystallization processes of $MAPbI_3$. On the other hand, the ionic Pb−Pb bonds are the longest among first nearest-neighbors, which suggests that they need to overcome some energy barriers to form the first nearest-neighbor Pb−Pb structural pairs. Such Pb−Pb structural pairs finally lead to the clustering of two or more neighboring PbI_6^{4-} octahedra, as shown in Figure 1d.

As shown in Figure 1c, we also observe that the second peak in the I−I RDF is located at ~6.2 Å (line 1), the same as the first peak in the Pb−Pb RDF but relatively broader, featuring not only the formation of PbI_6^{4-} octahedra, but also the

DOI: 10.1021/acs.cgd.7b00626
Cryst. Growth Des. 2017, 17, 6201−6211

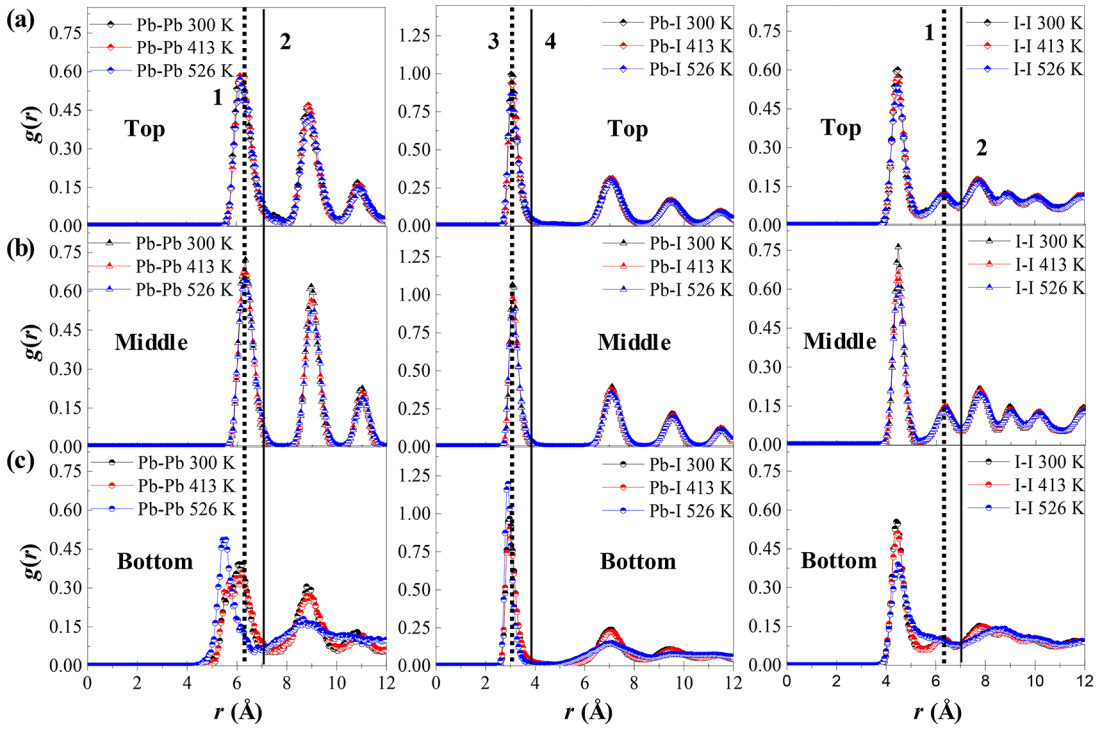

Figure 2. Normalized Pb−Pb (left), Pb−I (middle), and I−I (right) RDFs of the (a) top, (b) middle, and (c) bottom layer of a $MAPbI_3$ crystal interfacing with a TiO_2 substrate at 300, 413, and 526 K. The same vertical lines (1-4) shown in Figure 1c are also plotted here.

clustering among them. The second peak in the Pb−I RDF, which is more obvious than the second peak in the I−I RDF, is located closely to the first peak in the Pb−Pb RDF, reflecting the clustering of the neighboring PbI_6^{4-} octahedra. In general, both I−I and Pb−I RDFs exhibit primary peaks that are higher and sharper than the other ones, suggesting that the first nearest-neighbor I−I and Pb−I structural pairs are much more ordered and easier-forming than the others. Interestingly, the first peak in the Pb−Pb RDF is as high as the second one located at ∼8.9 Å, which characterizes the formation of unconnected PbI_6^{4-} octahedra along the diagonal of a cubic lattice of 8 PbI_6^{4-} octahedra. This suggests that, although adjacent corner-sharing octahedra are easy to form, the unconnected diagonal octahedra are almost as important as the connected corner-sharing ones in building the perovskite structure. On the basis of the above analysis, we can conclude that not only the second peaks in the I−I and Pb−I RDFs, but also the first and second peaks in the Pb−Pb RDF, play important roles (as fingerprints) in identifying structural features (such as early nuclei which we are interested in here) of a pristine bulk $MAPbI_3$ crystal.

3.2. Crystal Structure Evolution at the Perovskite−TiO_2 Interface. On the basis of its z-axis thickness in the perovskite−TiO_2 model system, the bulk $MAPbI_3$ crystal is divided into the bottom (z = 21−35 Å), middle (z = 40−54 Å), and top (z = 60−74 Å) layers (see Figure S2). Two relatively stable, charge-neutral free surfaces belonging to the bottom ($[PbI_2]^0$) and top ($[MAI]^0$) layers of $MAPbI_3$ are exposed to the (101) facets of the anatase TiO_2 slab, which produces two interfaces, as marked by $TiO_2/[PbI_2]^0$ and $TiO_2/[MAI]^0$. To characterize the $MAPbI_3$ structures at these two interfaces, we show the normalized Pb−Pb, Pb−I, and I−I RDFs in Figure 2 for the three layers at 300, 413, and 526 K. As shown in Figure 2b, the middle layer exhibits almost identical RDF patterns as those for the pristine bulk $MAPbI_3$ in Figure 1c, mainly due to the minor impact from the long-range interactions between them and the TiO_2 slab.

On the other hand, as shown from the RDFs in Figure 2a, the top $MAPbI_3$ layer (with the $TiO_2/[MAI]^0$ interface) exhibits structural features similar to those in the middle layer, which suggests that the $[MAI]^0$ surface is relative stable against TiO_2 at the temperatures considered. However, the top layer RDF peaks are slightly broadened compared to those in the middle layer, in particular for the Pb−Pb RDF. This finding is consistent with the observed defective region at the $TiO_2/[MAI]^0$ interface with a small gap between PbI_6^{4-} octahedra along the y-axis in the top layer (see Figure 3a ,b). The formation of this small gap is possibly due to the interactions between the $[MAI]^0$ layer and the TiO_2 slab, especially the electrostatic attractions between the I and Ti atoms at this interface.

Furthermore, we find that there are significant anisotropic lattice mismatches of $f_x = \frac{a_{MAPbI_3} - a_{TiO_2}}{a_{TiO_2}} = \frac{6.2\ Å - 3.8\ Å}{3.8\ Å} = 63\%$ and $f_y = \frac{c_{TiO_2} - a_{MAPbI_3}}{c_{TiO_2}} = \frac{9.5\ Å - 6.2\ Å}{9.5\ Å} = 31\%$ along the x and y-axis at the $TiO_2/[MAI]^0$ interface (see Figure 3b), respectively, without considering any potential crystallographic rotations or coincidence lattice mismatch. To estimate the theoretical lattice mismatch, we used the lattice constants for cubic $MAPbI_3$ (a_{MAPbI_3} = 6.2 Å, see Figure 1d) and tetragonal anatase (101) TiO_2 surface (a_{TiO_2} = 3.8 Å and c_{TiO_2} = 9.5 Å, see Figure S3), both determined from MD-simulated crystal structures at equilibrium. Such lattice mismatches could be reduced through edge dislocations in $MAPbI_3$ with one less or one extra lattice plane when one considers coincidence site lattices, e.g., with one less $MAPbI_3$ lattice plane every three TiO_2 lattices along the x-axis: $f_x = \frac{2 \times a_{MAPbI_3} - 3 \times a_{TiO_2}}{3 \times a_{TiO_2}} = \frac{2 \times 6.2\ Å - 3 \times 3.8\ Å}{3 \times 3.8\ Å} = 9\%$,

DOI: 10.1021/acs.cgd.7b00626
Cryst. Growth Des. 2017, 17, 6201−6211

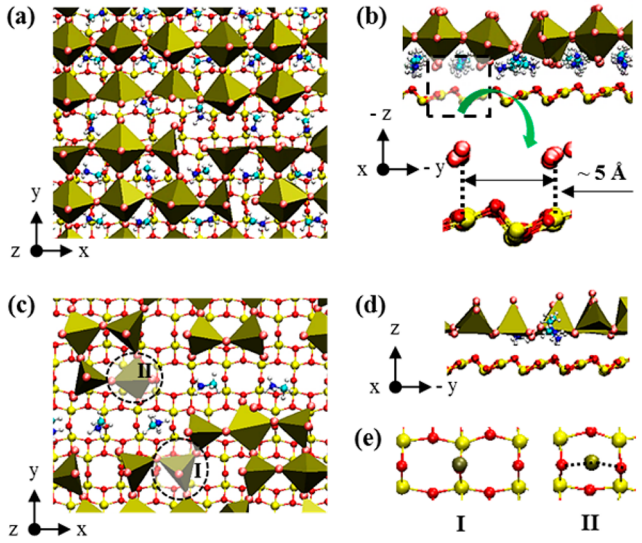

Figure 3. (a) Top and (b) side views of a defective region (showing Pb and I atoms with $z > 63$ Å, and MA^+ ions with $z > 67$ Å) in the top layer of the equilibrated $MAPbI_3$ crystal interfacing with a TiO_2 substrate at 526 K. Top (c) and side (d) views of a defective region ($z < 24$ Å) in the bottom layer of the equilibrated $MAPbI_3$ crystal interfacing with a TiO_2 substrate at 526 K. (e) Top view of two typical locations for the Pb atom sitting on the top of one neighboring surface O atom (marked as type I) or on the top of the midpoint between two neighboring surface O atoms (marked as type II). Color code: Ti − yellow, O − red, Pb − tan, I − pink, N − navy blue, C − light blue, H − white.

while with one extra $MAPbI_3$ lattice plane every two TiO_2 lattices along the y-axis: $f_y = \frac{2 \times c_{TiO_2} - 3 \times a_{MAPbI_3}}{2 \times c_{TiO_2}} = \frac{2 \times 9.5\ \text{Å} - 3 \times 6.2\ \text{Å}}{2 \times 9.5\ \text{Å}} = 2\%$. However, since the electrostatic attractions between I and Ti atoms are not very strong (e.g., compared to those between Pb and O atoms), such lattice mismatch can be easily accommodated by the small gap discussed above, as well as by the slight tilting and distortion of the PbI_6^{4-} octahedra.

On the other hand, Figure 2c shows that the RDFs in the bottom $MAPbI_3$ layer (near the $TiO_2/[PbI_2]^0$ interface) are significantly different from those in the top and middle layers. All the peaks in bottom layer RDFs, except for the first peak in the Pb−I RDF, are much broadened and lowered compared to the other layers. This reflects the defective structural nature of the $[PbI_2]^0$ surface at the three controlled temperatures. Some peaks are even unrecognizable, suggesting that many defects are formed at the $TiO_2/[PbI_2]^0$ interface. In addition, the shape changes of four typical fingerprinting RDF peaks, which are essential for identifying the crystal structure of $MAPbI_3$ as discussed earlier, are observed to be more significant at 526 K than the other two temperatures due to thermal fluctuation. For example, the second peak in the I−I RDF is merged into the first peak as a shoulder at 526 K, but just with a reduced height at 300 or 413 K; the second peaks in the Pb−I and Pb−Pb RDFs are also much more broadened and lowered at 526 K; the locations of the first peaks in the Pb−Pb RDFs are all red-shifted and reduced by up to 0.7 Å at 526 K.

On the basis of the above RDF analysis, we can conclude that the configuration of individual PbI_6^{4-} octahedra, as well as the cluster connections between the adjacent and diagonal octahedra at the $TiO_2/[PbI_2]^0$ interface, are significantly disordered. The MD snapshots from both the top and side views of a defective region in the bottom layer verify this (see Figure 3c,d). It is shown that the $[PbI_2]^0$ surface is destroyed so badly that even some MA^+ cations can move toward TiO_2 and reach the $TiO_2/[PbI_2]^0$ interface. Interestingly, most of the surface Pb atoms at the $TiO_2/[PbI_2]^0$ interface are constrained (and pulled away from their original locations in pristine $MAPbI_3$) to lattice locations close to the neighboring surface O atoms in TiO_2 due to strong electrostatic attractions. Two typical locations are shown in Figure 3e, where the Pb atom sits on the top of one neighboring surface O atom (marked as type I) or on the top of the midpoint between two neighboring surface O atoms (marked as type II). Therefore, we can conclude that the significant deformation of the $[PbI_2]^0$ surface is ascribed to the strong electrostatic attractions between Pb and O atoms at the $[PbI_2]^0/TiO_2$ interface. Because of the significant lattice mismatch, the strong electrostatic interactions lead to rearrangements of the Pb atoms to match the TiO_2 lattice, and eventually, the notable defects at the $TiO_2/[PbI_2]^0$ interface. In particular, such interactions could involve very strong electrostatic attractions between the Pb atoms on the $[PbI_2]^0$ surface and the surface O atoms from (101) anatase TiO_2. Therefore, we expect that the disordering of interfacial Pb atoms will affect the crystallization process of $MAPbI_3$ on the (101) anatase TiO_2 substrate under various synthesis environmental conditions.

3.3. Strong Precursor Composition-Dependent Pre-Nucleation. To understand the mechanisms behind the nucleus formation during the fabrication of hybrid perovskite films, we study the PVD process using a model system with PbI_2 and MAI precursor salts depositing onto a TiO_2 substrate (see Figure S1c) under three controlled temperatures (300, 413, and 526 K) and three precursor compositions (PbI_2/MAI = 1:2, 1:1, and 2:1, with the total number of salt molecules fixed). Considering that RDFs are not able to include bond orientation structures for a complex perovskite crystal, the nucleation processes under the above conditions are quantified by our in-house code using the Tool Command Language (Tcl) embedded in VMD.[53] To accurately identify and count early $MAPbI_3$ nuclei, we probe the atomic arrangements around each Pb atom, including the inorganic Pb−I framework composed of a connected network of PbI_6^{4-} octahedra as in bulk $MAPbI_3$, as well as the distribution of neighboring MA^+ cations. As shown in Figure 1a,b, each PbI_6^{4-} octahedron is surrounded by six first nearest-neighbor Pb atoms and eight first nearest-neighbor MA^+ cations. From the earlier RDF results in Figure 1c, the cutoff distance of the first nearest-neighbor Pb−I pairs in pristine bulk $MAPbI_3$ at 300 K is 3.7 Å, while it increases to 3.8 Å at 526 K due to thermal fluctuations. Similarly, the cutoff distance between adjacent PbI_6^{4-} octahedra, characterized by the first nearest-neighbor Pb−Pb structural pairs, is increased from 6.8 to 7.0 Å from 300 to 526 K due to thermal fluctuation. As shown in Figure S4, the cutoff distances of the first nearest-neighbor Pb−C and Pb−N structural pairs are increased to 6.6 and 6.8 Å, respectively, from 300 to 526 K. Here we employ the upper-bound cutoff distance values determined at 526 K to identify and quantify the populations of early nuclei after simulating the PVD process under each condition.

Interestingly, in addition to the typical full PbI_6^{4-} octahedra (see Figure 1d and Figure 4c) observed in a pristine bulk $MAPbI_3$ crystal, large amounts of under-coordinated PbI_x polyhedra, that is, the PbI_4^{2-} tetrahedra (see Figure 4a) and the PbI_5^{3-} pyramids (see Figure 4b), are also observed after the

DOI: 10.1021/acs.cgd.7b00626
Cryst. Growth Des. 2017, 17, 6201−6211

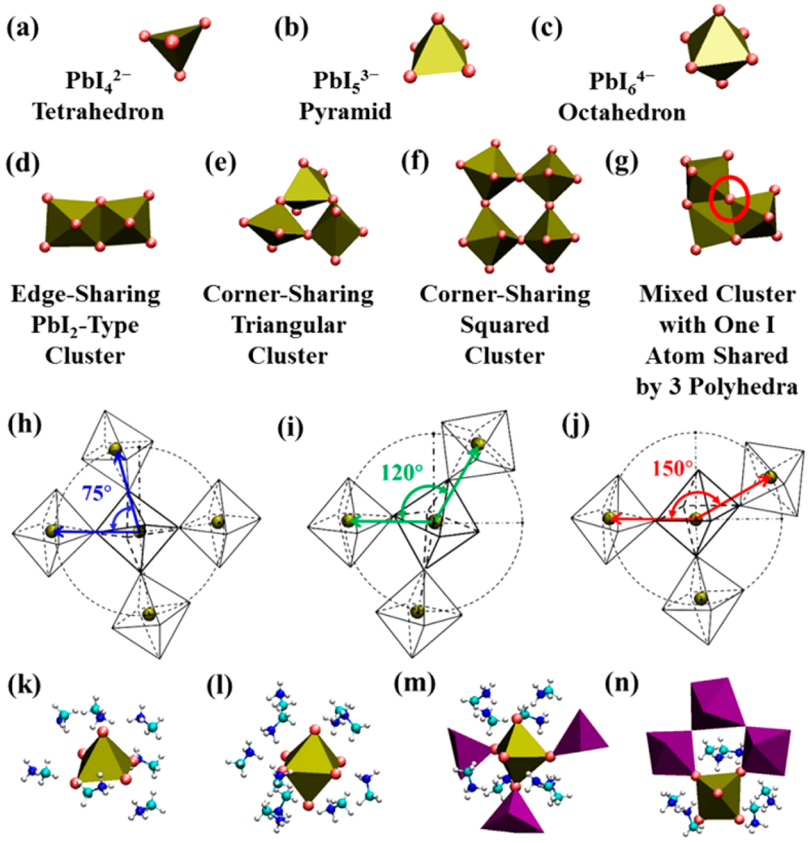

Figure 4. (a–c) Structures and definitions of three dominant PbI_x polyhedra during nucleation after vapor depositions: the PbI_4^{2-} tetrahedron, the PbI_5^{3-} pyramid, and the PbI_6^{4-} octahedron. The Pb atom is located at the center of each polyhedron. (d–f) Three typical arrangements of two adjacent polyhedra (within 7.0 Å of each other). In (d), two adjacent PbI_x polyhedra share two I atoms (edge-sharing) to form a PbI_2-type cluster. In (e), adjacent PbI_x polyhedra share only one I atom (corner-sharing) between each other, with three I atoms form vertices of a triangle to form a triangular cluster. (f) is similar to (e), but with the PbI_x polyhedra arranged into a squared lattice to form a squared cluster. In (g), a cluster built on both edge-sharing and corner-sharing PbI_x polyhedra with one I atom shared by three polyhedra. (h–j) Snapshots of three typical arrangements of PbI_x (x = 4, 5, and 6) polyhedra with critical vertex angles of (h) 75°, (i) 120°, and (j) 150° for a squared lattice. The PbI_6^{4-} octahedra are shown here as an example. (k–n) Four typical structures of the polyhedra considering the distribution of surrounding MA^+ cations and Pb-centered polyhedra (without showing I atoms on their vertices) for defining an early $MAPbI_3$ nucleus. The same color code used in Figure 3 is applied here.

PVD process. Furthermore, complicated arrangements of these three types of PbI_x polyhedra are observed from the simulated trajectories, such as (i) Pb–Pb pairs formed via edge sharing of two I atoms, similar to those in a typical PbI_2 crystal (considered as unfavorable PbI_2-type polyhedra for a perovskite structure, see Figure 4d) and (ii) Pb–Pb pairs formed via corner sharing of one I atom (considered as potentially well-connected PbI_x polyhedra for a perovskite structure, see Figure 4e,f). This makes it very challenging to study the structural characteristics of the deposited films and to further identify and distinguish different early $MAPbI_3$ nuclei. Indeed, using basic criteria from the distances and coordination numbers previously discussed is not accurate anymore to identify early nuclei. For example, the distances of the Pb–Pb pair between two adjacent corner-sharing PbI_6^{4-} octahedra in a $MAPbI_3$ crystal and the Pb–Pb pair between two adjacent edge-sharing PbI_6^{4-} octahedra in a typical PbI_2 crystal are very close to each other and difficult to differentiate, reflected from the obvious broadening of the first peaks in the Pb–Pb RDFs in Figure 2c. Accordingly, by taking the relative arrangements of adjacent PbI_x polyhedra into consideration as extra criteria, we classify these complex structures into three typical types of arrangements, as defined in Figure 4d–f.

To classify the arrangements of adjacent PbI_x polyhedra into different types, we define the α angle, which is the vertex angle between two vectors connecting a Pb atom with two adjacent Pb atoms in PbI_x polyhedra. As shown in Figure 4g–i, we then define triangular PbI_x clusters with $45° < \alpha < 75°$ and squared PbI_x clusters with $75° < \alpha < 120°$ or $150° < \alpha < 180°$. It should be noted that, as shown in Figure 4h,i, the α angles largely vary due to thermal fluctuation, especially when one Pb atom is missing on the vertices of a squared lattice. We first define the early $MAPbI_3$ nuclei as PbI_x clusters with well-connected PbI_x polyhedra without considering the distribution of the neighboring MA^+ cations. After analyzing MD trajectories after deposition, we define a Pb-centered PbI_4^{2-} tetrahedron as an early nucleus when this PbI_4^{2-} tetrahedron and its neighboring connected polyhedra form: (i) at least one corner-sharing squared cluster, (ii) no more than one PbI_2-type cluster, (iii) no triangular cluster, and (iv) no I atom shared by three polyhedra. Similarly, we define a Pb-centered PbI_5^{3-} pyramid as an early nucleus when this PbI_5^{3-} pyramid and its neighboring connected polyhedra form: (i) without any PbI_2-type cluster (or if there is one PbI_2-type cluster present, then there needs to be at least two corner-sharing clusters, in which at least one of them must belong to a squared cluster), (ii) no more than two triangular clusters, and (iii) no more

DOI: 10.1021/acs.cgd.7b00626
Cryst. Growth Des. 2017, 17, 6201–6211

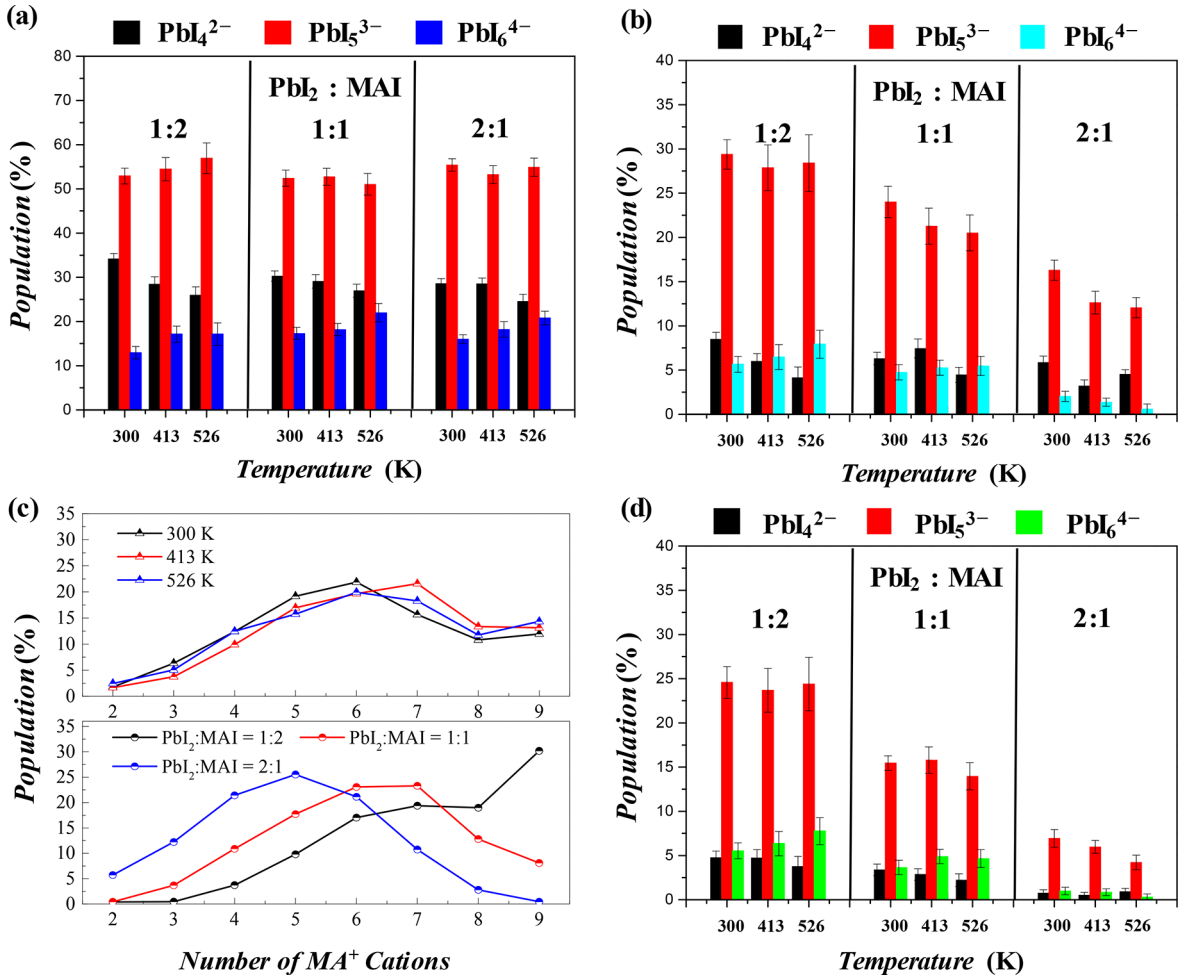

Figure 5. (a) Time-averaged populations of Pb atoms centered in three dominant PbI_x polyhedra under different precursor (MAI and PbI_2 salts) compositions and temperatures. The population is analyzed based on the structures shown in Figure 4a–c. (b) Time-averaged populations of Pb atoms centered in the three dominant well-connected PbI_x polyhedral clusters considering the Pb–I framework only. The corresponding population is analyzed based on the cluster structures shown in Figure 4d–f. (c) Time-averaged distributions of MA^+ cations within 6.6 (for Pb–C pairs) or 6.8 Å (for Pb–N pairs) around the Pb atoms in three dominant types of well-connected PbI_x polyhedral clusters as in (b), averaged over different precursor compositions (top) and temperatures (bottom). (d) Time-averaged populations of Pb atoms centered in efficient early $MAPbI_3$ nuclei, considering surrounding MA^+ distributions around PbI_x polyhedral clusters in (b). The population is analyzed based on the structures shown in Figure 4j–m. All the error bars represent the standard deviations of the time-averaged data.

than one I atom shared by three polyhedra. Finally, we define a Pb-centered PbI_6^{4-} octahedron as an early nucleus when this PbI_6^{4-} octahedron and its neighboring connected polyhedra form the same structure as that for defining a PbI_5^{3-} pyramid-based early nucleus. Many badly connected clusters are excluded from these criteria, as shown in Figure S5 for PbI_6^{4-} octahedra-based clusters.

In Figure 5a,b, we report the time-averaged populations of Pb atoms (in percentage, normalized by the total number of Pb atoms in the system) in PbI_x (x = 3, 4, and 5) polyhedra and well-connected PbI_x polyhedra clusters as early $MAPbI_3$ nuclei, respectively, after vapor deposition processes under various conditions. Figure 5a is obtained using a cutoff distance of 3.8 Å (the maximum Pb–I bond length at 526 K) between central Pb atoms and surrounding I atoms. We find that the PbI_5^{3-} pyramids account for over 52% of the Pb atoms under all the conditions, revealing that the PbI_5^{3-} pyramids are dominant and easier to form than other types of polyhedra, which could be a very competitive candidate to convert into PbI_6^{4-} octahedra upon further crystallization. Moreover, the PbI_4^{2-} tetrahedra account for at least 24% of the Pb atoms, more than that of the PbI_6^{4-} octahedra, partly because the upper region of the deposited film is not as dense as other regions in the systems. Notably, higher temperatures seem to help the formation of PbI_6^{4-} octahedra under all defined compositions, possibly due to the accelerated nucleation kinetics via faster ion diffusions.[54] In accordance, we find that less PbI_4^{2-} tetrahedra are generated with increasing temperature. However, the influences from temperature seem to be weaker on the populations of PbI_5^{3-} pyramids, where an obvious upward trend with increasing temperature is observed only at a precursor composition of PbI_2/MAI = 1:2.

On the other hand, in Figure 5b, the populations of well-connected PbI_x clusters (as early $MAPbI_3$ nuclei) depend more on the precursor composition than the PbI_x polyhedra in Figure 5a. Furthermore, after considering the above connectivity criteria, polyhedra-based PbI_x clusters exhibit much a lower population than those for PbI_x polyhedra under all temperature and precursor composition conditions. Specifically, under a composition of PbI_2/MAI = 2:1, the populations of the PbI_x clusters are generally decreased (by over 14%, and in particular, up to 42% for the PbI_5^{3-} pyramids, both in absolute values),

DOI: 10.1021/acs.cgd.7b00626
Cryst. Growth Des. 2017, 17, 6201–6211

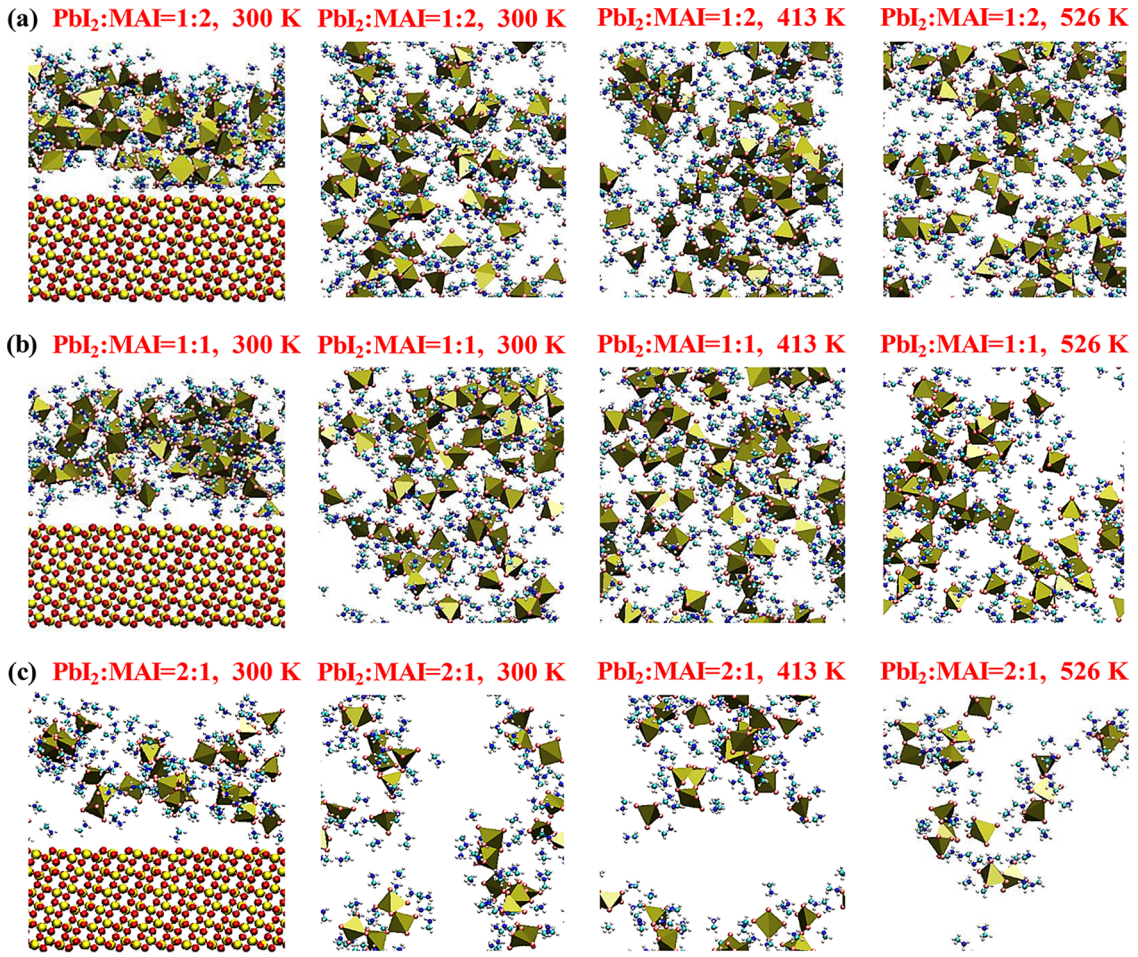

Figure 6. MD simulation snapshots of efficient early $MAPbI_3$ nuclei identified (via the typical structures in Figure 4j–m and corresponding to the populations in Figure 5d) at 40 ns after the vapor deposition processes at three controlled temperatures (300, 413, and 526 K) and three precursor compositions (PbI_2/MAI = 1:2, 1:1, and 2:1, with the total number of salt molecules fixed). Note that amorphous, completely disordered $MAPbI_3$ species (MA^+, I^-, and Pb^{2+}) that do not belong to the early $MAPbI_3$ nuclei are not shown for clarity.

suggesting that only few PbI_x polyhedra meet these connectivity criteria to become early $MAPbI_3$ nuclei. Meanwhile, the decreases in the populations of the PbI_5^{3-} pyramids and PbI_6^{4-} octahedra in PbI_x clusters under a composition of PbI_2/MAI = 1:1 are much higher than those under PbI_2/MAI = 1:2, *vice versa* for the PbI_4^{2-} tetrahedra in PbI_x clusters. In general, despite such a decrease, the population of the PbI_5^{3-} pyramids in PbI_x clusters is even more dominant and higher than the sum of the other two polyhedra in PbI_x clusters. However, unlike populations of individual polyhedra in Figure 5a, the population of PbI_4^{2-} tetrahedra in PbI_x clusters is less than that of PbI_6^{4-} octahedra in PbI_x clusters at 413 and 526 K under compositions of PbI_2/MAI = 1:2, while the similar trend only exists at 526 K under compositions of PbI_2/MAI = 1:1. Notably, a downward trend is observed in the populations of PbI_5^{3-} pyramids in PbI_x clusters when increasing the temperature or the composition of PbI_2/MAI.

Finally, we account for the distributions of the MA^+ cations around the above three types of well-connected PbI_x polyhedral clusters to understand how $MAPbI_3$ prenucleation depends on precursor composition and temperature. We calculated and compared the number of MA^+ cations around Pb atoms (see Figure S6) within a cutoff distance of 6.6 Å (for Pb–C pairs) or 6.8 Å (for Pb–N pairs), based on the corresponding RDFs shown in Figure S4 under different precursor compositions and temperatures. As shown in Figure 5c, the distributions are averaged over different compositions and temperatures, which exhibit a maximum probability to have 5–7 MA^+ cations around a Pb atom. On the basis of this distribution, we define PbI_x polyhedral clusters with more than five MA^+ cations around them as efficient early $MAPbI_3$ nuclei and report the time-averaged distributions of Pb atoms belonging to these efficient early nuclei in Figure 5d. The identified efficient early $MAPbI_3$ nuclei, defined by well-connected PbI_x polyhedral clusters (with more corner-sharing lattices as potential nuclei formers) and sufficient neighboring MA^+ cations, are illustrated in Figure 6 under various temperatures and precursor compositions. The simulated systems are confirmed to reach kinetic equilibrium by monitoring the time-evolution of the above distributions in Figure S7.

As shown in Figure 5d, the normalized populations of the PbI_x polyhedra in efficient early $MAPbI_3$ nuclei decrease rapidly with increasing the precursor composition PbI_2/MAI at all the temperatures, suggesting potential improvements of the film quality and crystal structure upon depositing more MAI salts into the system. This finding is in good agreement with the experimental observation by Snaith et al.[22] Moreover, we also notice that with more MA^+ cations or MAI salts added, the identified early nuclei are composed of more squared clusters (good nucleus formers) and less PbI_2-type clusters (bad

DOI: 10.1021/acs.cgd.7b00626
Cryst. Growth Des. 2017, 17, 6201–6211

nucleus formers), which we believe would further benefit the formation of efficient Pb−I framework for $MAPbI_3$ crystallization. However, the differences among the populations of Pb atoms in these efficient early $MAPbI_3$ nuclei at different temperatures are quite small compared to those under different precursor compositions. Therefore, we can conclude that the precursor composition PbI_2/MAI plays a more important role than temperature on the prenucleation of crystalline $MAPbI_3$ using the PVD method. In general, the intermediate temperature of 413 K leads to the most amount of efficient early $MAPbI_3$ nuclei with a precursor composition PbI_2/MAI = 1:1, while temperatures of 526 and 300 K lead to the largest amount of efficient early $MAPbI_3$ nuclei under precursor compositions of PbI_2/MAI = 1:2 and 2:1, respectively. Similar to the populations of PbI_5^{3-} pyramids and PbI_5^{3-}-centered clusters in Figure 5a,b, PbI_5^{3-} pyramids in early $MAPbI_3$ nuclei are also dominant under all the conditions, suggesting that the PbI_5^{3-} pyramids are not only the easiest to form, but also the easiest to build early nuclei around them during the early stage of crystallization, which could be very competitive to evolve into PbI_6^{4-} octahedra upon further crystallization. In addition, although the population of PbI_4^{2-} tetrahedra is higher than that of PbI_6^{4-} octahedra (see Figure 5a), the former is less than the later in the identified early nuclei (see Figure 5d), since a smaller amount of MA^+ cations tends to surround the PbI_4^{2-} tetrahedra, especially under compositions of PbI_2/MAI = 1:1 and 1:2 (see Figure S6).

On the other hand, as shown in Figure 5d, the differences among the populations of Pb atoms in efficient early $MAPbI_3$ nuclei at different temperatures are quite small compared to those under different precursor compositions, suggesting their weaker influence on nucleus formation of crystalline $MAPbI_3$ by the PVD method. Under the composition of PbI_2/MAI = 1:2, the population of PbI_6^{4-} octahedra in early nuclei gradually increases with elevating temperature, while the populations of the other two polyhedra in early nuclei do not exhibit any clear trend. This implies that under this composition, the deposited film at the higher 526 K has a relatively better quality in terms of the PbI_6^{4-} octahedra. However, under the composition of PbI_2/MAI = 2:1, the higher temperature of 526 K seems to impede the generation of efficient early $MAPbI_3$ nuclei, possibly due to thermally activated Pb diffusions which could enhance the formation of edge-sharing PbI_6^{4-} octahedra (typical in a PbI_2 crystal) with fewer MA^+ cations around them. For example, the population of the early nuclei at 526 K is over 2% (in absolute value) or 26% (in relative value) less than those at 300 and 413 K.

Finally, in Figures S8 and S9 we report the impacts from the TiO_2 substrate on the distributions of ionic species, including Pb^{2+}, I^-, and MA^+, as well as the Pb atoms in efficient early $MAPbI_3$ nuclei after the vapor deposition processes. We find that the TiO_2 substrate can promote ordering of layered ionic structures close to its surface; however, it does not significantly promote the prenucleation of $MAPbI_3$. On one hand, those ionic species accumulate at the TiO_2 surface and exhibit an ordered layer-by-layer structure very close to the TiO_2 surface ($z < 20$ Å), where each layer is separated by around 5, 3, and 5 Å for Pb^{2+}, I^- and MA^+, respectively. This phenomenon is primarily due to geometrical confinement and strong absorptions and the combined LJ and electrostatic interactions between TiO_2 and the ionic species. Meanwhile, the ionic and early nuclei distribution depend only weakly on temperature and PbI_2/MAI composition.

On the other hand, the TiO_2 substrate does not significantly promote the interface-originated prenucleation of $MAPbI_3$, but still seems to contribute to the formation of more PbI_5^{3-}-based early nuclei under the composition of PbI_2/MAI = 1:2. This is probably due to the stronger electrostatic attractions between Pb atoms which are more exposed in a PbI_5^{3-} pyramid structure (while they are enveloped by neighboring I atoms in tetragonal PbI_4^{2-} and octahedral PbI_6^{4-} structures) and surface O atoms of TiO_2. This could lead to the formation of more PbI_5^{3-} pyramids on the TiO_2 surface (see Figure 6a) and therefore, higher populations of PbI_5^{3-}-based early nuclei close to that surface.

4. CONCLUSIONS

In summary, we reported a systematic MD simulation study of ionic precursor composition and temperature-dependent prenucleation and interfacial mismatch during vapor deposition of hybrid perovskite $MAPbI_3$ on a TiO_2 substrate. Despite significant anisotropic lattice mismatches at the $MAPbI_3$−TiO_2 interface, the intermediate electrostatic attractions between I and Ti atoms lead to small gap formation and distortion of PbI_6^{4-} octahedra at the TiO_2/$[MAI]^0$ interface. On the other hand, very strong electrostatic attractions between Pb and O atoms lead to significant rearrangements of the Pb atoms and defect formation at the TiO_2/$[PbI_2]^0$ interface. According to our PVD simulations, three dominant polyhedral building blocks of early $MAPbI_3$ nuclei exist in the deposited films under all of the above conditions, including (i) the PbI_4^{2-} tetrahedra, (ii) PbI_5^{3-} pyramids, and (iii) the characteristic PbI_6^{4-} octahedra, which better resemble pristine perovskite structures. Specifically, the PbI_5^{3-} pyramids account for the majority among all these polyhedra and could be a very good candidate for converting into the PbI_6^{4-} octahedra upon further crystallization.

Moreover, very complicated arrangements of these polyhedra have been observed, which makes it challenging to categorize $MAPbI_3$ nuclei into different types. We further quantify the populations of PbI_x (x = 4, 5, and 6) polyhedra in well-connected clusters, also considering the distribution of MA^+ cations around them within certain cutoff distances. On the basis of these measurements, we identify various types of early $MAPbI_3$ nuclei built upon PbI_x and observe strong dependence of their populations and distributions on the ionic precursor composition. The populations of efficient early $MAPbI_3$ nuclei increase rapidly with increasing the MAI composition at all temperatures, suggesting that potential improvements in film qualities could be introduced by depositing more MAI salts into the system. We also found that the impacts from the temperature on the populations of different early nuclei are weaker than those from the precursor composition.

Finally, we found that the TiO_2 substrate leads to layered structures of the ionic species close to the TiO_2 surface due to geometrical confinement and stronger adsorptions of these species from the combined LJ and electrostatic interactions, rather than the temperature and PbI_2/MAI composition. However, such ordering does not promote the formation of early $MAPbI_3$ nuclei at the TiO_2 surface. But the formation of more efficient PbI_5^{3-}-based early nuclei under the composition of PbI_2/MAI = 1:2 seems to originate from the stronger electrostatic attractions between the more exposed Pb atoms in a pyramid structure and surface O atoms of TiO_2.

Other organic cations such as formamidinium (FA^+) or halide anions such as Br^- have been involved in the fabrication

DOI: 10.1021/acs.cgd.7b00626
Cryst. Growth Des. 2017, 17, 6201−6211

of PSCs with PCEs over 20%,[16] suggesting the strong impact from the molecular nature of the ionic species on nucleation and film quality. Therefore, future studies would involve these new ionic components or explore the vapor-assisted solution methods to investigate fundamental mechanisms behind perovskite nucleation in more advanced fabrication techniques. We believe that the MD simulation work presented here will serve as a guideline for identifying the key prenucleation clusters during perovskite crystallization, which could be very useful for explaining experimental observations. The extension of the nuclei structural model and data analysis protocol here to other pure or mixed-ion hybrid perovskite systems depends on their crystal structures and the primary unfavorable polyhedra structures (e.g., the easily formed but unfavorable PbI_2 crystals during $MAPbI_3$ nucleation might be absent in other perovskite systems). This work can also serve as a first step (collective-variable design for order parameters) toward rare-event sampling techniques for quantifying the free energy of perovskite crystallization, such as metadynamics,[55] umbrella sampling,[56] and Monte Carlo simulations.[57]

■ ASSOCIATED CONTENT

Supporting Information

The Supporting Information is available free of charge on the ACS Publications website at DOI: 10.1021/acs.cgd.7b00626.

Supporting Figures S1−S9 and Table S1 (PDF)

■ AUTHOR INFORMATION

Corresponding Authors

*(L.Z.) Phone: (86) 138 5168 0995. E-mail: zhao_lingling@seu.edu.cn.

*(S.L.) Phone: (850) 645 0138. E-mail: slin@eng.famu.fsu.edu.

ORCID

Lingling Zhao: 0000-0002-1532-7247

Shangchao Lin: 0000-0002-6810-1380

Notes

The authors declare no competing financial interest.

■ ACKNOWLEDGMENTS

S.L. and M.W. would like to acknowledge startup funding from the Energy and Materials Initiative from the Florida State University and funding from the National Science Foundation (NSF-CBET-1708968). L.Z. and J.W. would like to acknowledge funding from the National Natural Science Foundation of China (Grant No. 51106027).

■ REFERENCES

(1) Stranks, S. D.; Snaith, H. J. Metal-Halide Perovskites for Photovoltaic and Light-Emitting Devices. *Nat. Nanotechnol.* **2015**, *10*, 391−402.

(2) Green, M. A.; Ho-Baillie, A.; Snaith, H. J. The Emergence of Perovskite Solar Cells. *Nat. Photonics* **2014**, *8*, 506−514.

(3) Gratzel, M. The Light and Shade of Perovskite Solar Cells. *Nat. Mater.* **2014**, *13*, 838−842.

(4) He, Y.; Galli, G. Perovskites for Solar Thermoelectric Applications: A First Principle Study of $Ch_3nh_3ai_3$ (a = Pb and Sn). *Chem. Mater.* **2014**, *26*, 5394−5400.

(5) Mettan, X.; Pisoni, R.; Matus, P.; Pisoni, A.; Jaćimović, J.; Náfrádi, B.; Spina, M.; Pavuna, D.; Forró, L.; Horváth, E. Tuning of the Thermoelectric Figure of Merit of $Ch_3nh_3mi_3$ (M = Pb,Sn) Photovoltaic Perovskites. *J. Phys. Chem. C* **2015**, *119*, 11506−11510.

(6) Xing, G. C.; Mathews, N.; Sun, S. Y.; Lim, S. S.; Lam, Y. M.; Gratzel, M.; Mhaisalkar, S.; Sum, T. C. Long-Range Balanced Electron- and Hole-Transport Lengths in Organic-Inorganic $Ch_3nh_3pbi_3$. *Science* **2013**, *342*, 344−347.

(7) Pisoni, A.; Jaćimović, J.; Barišić, O. S.; Spina, M.; Gaál, R.; Forró, L.; Horváth, E. Ultra-Low Thermal Conductivity in Organic−Inorganic Hybrid Perovskite $Ch_3nh_3pbi_3$. *J. Phys. Chem. Lett.* **2014**, *5*, 2488−2492.

(8) Chen, Q.; Zhou, H.; Hong, Z.; Luo, S.; Duan, H. S.; Wang, H. H.; Liu, Y.; Li, G.; Yang, Y. Planar Heterojunction Perovskite Solar Cells Via Vapor-Assisted Solution Process. *J. Am. Chem. Soc.* **2014**, *136*, 622−5.

(9) Giordano, F.; Abate, A.; Correa Baena, J. P.; Saliba, M.; Matsui, T.; Im, S. H.; Zakeeruddin, S. M.; Nazeeruddin, M. K.; Hagfeldt, A.; Graetzel, M. Enhanced Electronic Properties in Mesoporous Tio2 Via Lithium Doping for High-Efficiency Perovskite Solar Cells. *Nat. Commun.* **2016**, *7*, 10379.

(10) Heo, J. H.; et al. Efficient Inorganic−Organic Hybrid Heterojunction Solar Cells Containing Perovskite Compound and Polymeric Hole Conductors. *Nat. Photonics* **2013**, *7*, 486−491.

(11) Jeon, N. J.; Noh, J. H.; Kim, Y. C.; Yang, W. S.; Ryu, S.; Seok, S. I. Solvent Engineering for High-Performance Inorganic-Organic Hybrid Perovskite Solar Cells. *Nat. Mater.* **2014**, *13*, 897−903.

(12) Jeon, N. J.; Noh, J. H.; Yang, W. S.; Kim, Y. C.; Ryu, S.; Seo, J.; Seok, S. I. Compositional Engineering of Perovskite Materials for High-Performance Solar Cells. *Nature* **2015**, *517*, 476−80.

(13) Seo, J.; Noh, J. H.; Seok, S. I. Rational Strategies for Efficient Perovskite Solar Cells. *Acc. Chem. Res.* **2016**, *49*, 562−72.

(14) Wu, Y.; Islam, A.; Yang, X.; Qin, C.; Liu, J.; Zhang, K.; Peng, W.; Han, L. Retarding the Crystallization of Pbi_2 for Highly Reproducible Planar-Structured Perovskite Solar Cells Via Sequential Deposition. *Energy Environ. Sci.* **2014**, *7*, 2934.

(15) NREL Efficiency Chart, https://www.nrel.gov/pv/assets/images/efficiency-chart.png.

(16) Nie, W. Y.; et al. High-Efficiency Solution-Processed Perovskite Solar Cells with Millimeter-Scale Grains. *Science* **2015**, *347*, 522−525.

(17) Zhou, H.; Chen, Q.; Li, G.; Luo, S.; Song, T.-b.; Duan, H.-S.; Hong, Z.; You, J.; Liu, Y.; Yang, Y. Interface Engineering of Highly Efficient Perovskite Solar Cells. *Science* **2014**, *345*, 542−546.

(18) Ardo, S.; Meyer, G. J. Photodriven Heterogeneous Charge Transfer with Transition-Metal Compounds Anchored to Tio_2 Semiconductor Surfaces. *Chem. Soc. Rev.* **2009**, *38*, 115−64.

(19) Hardin, B. E.; Snaith, H. J.; McGehee, M. D. The Renaissance of Dye-Sensitized Solar Cells. *Nat. Photonics* **2012**, *6*, 162−169.

(20) De Wolf, S.; Holovsky, J.; Moon, S. J.; Loper, P.; Niesen, B.; Ledinsky, M.; Haug, F. J.; Yum, J. H.; Ballif, C. Organometallic Halide Perovskites: Sharp Optical Absorption Edge and Its Relation to Photovoltaic Performance. *J. Phys. Chem. Lett.* **2014**, *5*, 1035−9.

(21) Conibeer, G. Third-Generation Photovoltaics. *Mater. Today* **2007**, *10*, 42−50.

(22) Liu, M.; Johnston, M. B.; Snaith, H. J. Efficient Planar Heterojunction Perovskite Solar Cells by Vapour Deposition. *Nature* **2013**, *501*, 395−8.

(23) Luo, P.; Liu, Z.; Xia, W.; Yuan, C.; Cheng, J.; Lu, Y. Uniform, Stable, and Efficient Planar-Heterojunction Perovskite Solar Cells by Facile Low-Pressure Chemical Vapor Deposition under Fully Open-Air Conditions. *ACS Appl. Mater. Interfaces* **2015**, *7*, 2708−14.

(24) Eperon, G. E.; Burlakov, V. M.; Docampo, P.; Goriely, A.; Snaith, H. J. Morphological Control for High Performance, Solution-Processed Planar Heterojunction Perovskite Solar Cells. *Adv. Funct. Mater.* **2014**, *24*, 151−157.

(25) Rong, Y.; Tang, Z.; Zhao, Y.; Zhong, X.; Venkatesan, S.; Graham, H.; Patton, M.; Jing, Y.; Guloy, A. M.; Yao, Y. Solvent Engineering Towards Controlled Grain Growth in Perovskite Planar Heterojunction Solar Cells. *Nanoscale* **2015**, *7*, 10595−9.

(26) Hu, L.; et al. Sequential Deposition of $Ch_3nh_3pbi_3$ on Planar Nio Film for Efficient Planar Perovskite Solar Cells. *ACS Photonics* **2014**, *1*, 547−553.

(27) Bonaccorso, F.; Colombo, L.; Yu, G.; Stoller, M.; Tozzini, V.; Ferrari, A. C.; Ruoff, R. S.; Pellegrini, V. 2d Materials. Graphene,

Related Two-Dimensional Crystals, and Hybrid Systems for Energy Conversion and Storage. *Science* **2015**, *347*, 1246501.
(28) Muccioli, L.; D'Avino, G.; Zannoni, C. Simulation of Vapor-Phase Deposition and Growth of a Pentacene Thin Film on C60 (001). *Adv. Mater.* **2011**, *23*, 4532−6.
(29) Reineke, S.; Lindner, F.; Schwartz, G.; Seidler, N.; Walzer, K.; Lussem, B.; Leo, K. White Organic Light-Emitting Diodes with Fluorescent Tube Efficiency. *Nature* **2009**, *459*, 234−8.
(30) Werner, J.; Weng, C. H.; Walter, A.; Fesquet, L.; Seif, J. P.; De Wolf, S.; Niesen, B.; Ballif, C. Efficient Monolithic Perovskite/Silicon Tandem Solar Cell with Cell Area > 1 Cm^2. *J. Phys. Chem. Lett.* **2016**, *7*, 161−6.
(31) Plimpton, S. Fast Parallel Algorithms for Short-Range Molecular Dynamics. *J. Comput. Phys.* **1995**, *117*, 1−19.
(32) Mattoni, A.; Filippetti, A.; Saba, M. I.; Delugas, P. Methylammonium Rotational Dynamics in Lead Halide Perovskite by Classical Molecular Dynamics: The Role of Temperature. *J. Phys. Chem. C* **2015**, *119*, 17421−17428.
(33) Delugas, P.; Caddeo, C.; Filippetti, A.; Mattoni, A., Thermally Activated Point-Defects Diffusion in Methylammonium Lead Trihalide: Anisotropic and Ultra-High Mobility of Iodine. *J. Phys. Chem. Lett.* **2016**.7235610.1021/acs.jpclett.6b00963
(34) Mattoni, A.; Filippetti, A.; Saba, M. I.; Caddeo, C.; Delugas, P. Temperature Evolution of Methylammonium Trihalide Vibrations at the Atomic Scale. *J. Phys. Chem. Lett.* **2016**, *7*, 529−535.
(35) Yang, L.; Barrows, A. T.; Lidzey, D. G.; Wang, T. Recent Progress and Challenges of Organometal Halide Perovskite Solar Cells. *Rep. Prog. Phys.* **2016**, *79*, 026501.
(36) Caddeo, C.; Melis, C.; Saba, M. I.; Filippetti, A.; Colombo, L.; Mattoni, A. Tuning the Thermal Conductivity of Methylammonium Lead Halide by the Molecular Substructure. *Phys. Chem. Chem. Phys.* **2016**, *18*, 24318−24324.
(37) Liu, S.; Cohen, R. E. Response of Methylammonium Lead Iodide to External Stimuli and Caloric Effects from Molecular Dynamics Simulations. *J. Phys. Chem. C* **2016**, *120*, 17274−17281.
(38) Yu, J.; Wang, M.; Lin, S. Probing the Soft and Nanoductile Mechanical Nature of Single and Polycrystalline Organic−Inorganic Hybrid Perovskites for Flexible Functional Devices. *ACS Nano* **2016**, *10*, 11044−11057.
(39) Bourikas, K.; Kordulis, C.; Lycourghiotis, A. Titanium Dioxide (Anatase and Rutile): Surface Chemistry, Liquid-Solid Interface Chemistry, and Scientific Synthesis of Supported Catalysts. *Chem. Rev.* **2014**, *114*, 9754−823.
(40) Matsui, M.; Akaogi, M. Molecular Dynamics Simulation of the Structural and Physical Properties of the Four Polymorphs of TiO_2. *Mol. Simul.* **1991**, *6*, 239−244.
(41) Oliver, P. M.; Watson, G. W.; Kelsey, E.; Parker, S. C. Atomistic Simulation of the Surface Structure of the TiO_2 Polymorphs Rutile and Anatase. *J. Mater. Chem.* **1997**, *7*, 563−568.
(42) Ponder, J. W.; Case, D. A., Force Fields for Protein Simulations. In *Advances in Protein Chemistry*; Academic Press, 2003; Vol. *66*, pp 27−85.
(43) Li, P.; Roberts, B. P.; Chakravorty, D. K.; Merz, K. M., Jr. Rational Design of Particle Mesh Ewald Compatible Lennard-Jones Parameters for + 2 Metal Cations in Explicit Solvent. *J. Chem. Theory Comput.* **2013**, *9*, 2733−2748.
(44) McDonald, N. A.; Duffy, E. M.; Jorgensen, W. L. Monte Carlo Investigations of Selective Anion Complexation by a Bis (Phenylurea) P-Tert-Butylcalix [4] Arene. *J. Am. Chem. Soc.* **1998**, *120*, 5104−5111.
(45) Rappé, A. K.; Casewit, C. J.; Colwell, K.; Goddard, W. A.; Skiff, W. Uff, a Full Periodic Table Force Field for Molecular Mechanics and Molecular Dynamics Simulations. *J. Am. Chem. Soc.* **1992**, *114*, 10024−10035.
(46) Essmann, U.; Perera, L.; Berkowitz, M. L.; Darden, T.; Lee, H.; Pedersen, L. G.; Smooth, A. Particle Mesh Ewald Method. *J. Chem. Phys.* **1995**, *103*, 8577−8593.
(47) Darden, T.; York, D.; Pedersen, L. Particle Mesh Ewald: An N Log(N) Method for Ewald Sums in Large Systems. *J. Chem. Phys.* **1993**, *98*, 10089−10092.
(48) Nosé, S. A Unified Formulation of the Constant Temperature Molecular Dynamics Methods. *J. Chem. Phys.* **1984**, *81*, 511−519.
(49) Hoover, W. G. Canonical Dynamics: Equilibrium Phase-Space Distributions. *Phys. Rev. A: At., Mol., Opt. Phys.* **1985**, *31*, 1695−1697.
(50) Leguy, A. M.; et al. The Dynamics of Methylammonium Ions in Hybrid Organic-Inorganic Perovskite Solar Cells. *Nat. Commun.* **2015**, *6*, 7124.
(51) Weller, M. T.; Weber, O. J.; Henry, P. F.; Di Pumpo, A. M.; Hansen, T. C. Complete Structure and Cation Orientation in the Perovskite Photovoltaic Methylammonium Lead Iodide between 100 and 352 K. *Chem. Commun.* **2015**, *51*, 4180−3.
(52) Frost, J. M.; Butler, K. T.; Walsh, A. Molecular Ferroelectric Contributions to Anomalous Hysteresis in Hybrid Perovskite Solar Cells. *APL Mater.* **2014**, *2*, 081506.
(53) Humphrey, W.; Dalke, A.; Schulten, K. Vmd: Visual Molecular Dynamics. *J. Mol. Graphics* **1996**, *14*, 33−38.
(54) Carlson, W. D. The Significance of Intergranular Diffusion to the Mechanisms and Kinetics of Porphyroblast Crystallization. *Contrib. Mineral. Petrol.* **1989**, *103*, 1−24.
(55) Quigley, D.; Rodger, P. M. A Metadynamics-Based Approach to Sampling Crystallisation Events. *Mol. Simul.* **2009**, *35*, 613−623.
(56) ten Wolde, P. R.; Ruiz-Montero, M. J.; Frenkel, D. Numerical Evidence for Bcc Ordering at the Surface of a Critical Fcc Nucleus. *Phys. Rev. Lett.* **1995**, *75*, 2714−2717.
(57) Radhakrishnan, R.; Trout, B. L. Nucleation of Crystalline Phases of Water in Homogeneous and Inhomogeneous Environments. *Phys. Rev. Lett.* **2003**, *90*, 158301.

DOI: 10.1021/acs.cgd.7b00626
Cryst. Growth Des. 2017, 17, 6201−6211